



Cite this: *Chem. Sci.*, 2023, **14**, 12570

All publication charges for this article have been paid for by the Royal Society of Chemistry

## Controllable synthesis of a Na-enriched $\text{Na}_4\text{V}_2(\text{PO}_4)_3$ cathode for high-energy sodium-ion batteries: a redox-potential-matched chemical sodiation approach<sup>†</sup>

Mingli Xu,<sup>a</sup> Fengxue Zhang,<sup>b</sup> Yanhui Zhang,<sup>b</sup> Chen Wu,<sup>a</sup> Xue Zhou,<sup>c</sup> Xinping Ai<sup>ID a</sup> and Jiangfeng Qian<sup>ID \*a</sup>

Exploring a sodium-enriched cathode (i.e.  $\text{Na}_4\text{V}_2(\text{PO}_4)_3$ , which differs from its traditional stoichiometric counterpart  $\text{Na}_3\text{V}_2(\text{PO}_4)_3$ ) that can provide extra endogenous sodium reserves to mitigate the irreversible capacity loss of the anode material (i.e. hard carbon), is an intriguing presodiation method for the development of high energy sodium-ion batteries. To meet this challenge, herein, we first propose a redox-potential-matched chemical sodiation approach, utilizing phenazine-sodium (PNZ-Na) as the optimal reagent to sodiate the  $\text{Na}_3\text{V}_2(\text{PO}_4)_3$  precursor into Na-enriched  $\text{Na}_4\text{V}_2(\text{PO}_4)_3$ . The spontaneous sodiation reaction enables a fast reduction of one-half V ions from  $\text{V}^{3+}$  to  $\text{V}^{2+}$ , followed by the insertion of one  $\text{Na}^+$  ion into the NASICON framework, which only takes 90 s to obtain the phase-pure  $\text{Na}_4\text{V}_2(\text{PO}_4)_3$  product. When paired with a hard carbon anode, the resulting  $\text{Na}_4\text{VP}||\text{HC}$  full cell exhibits a high energy density of  $251 \text{ W h kg}^{-1}$ , which is 58% higher than that of  $159 \text{ W h kg}^{-1}$  for the  $\text{Na}_3\text{VP}||\text{HC}$  control cell. Our chemical sodiation methodology provides an innovative approach for designing sodium-rich cathode materials and could serve as an impetus to the development of advanced sodium-ion batteries.

Received 8th July 2023  
Accepted 24th October 2023

DOI: 10.1039/d3sc03498d  
[rsc.li/chemical-science](http://rsc.li/chemical-science)

## Introduction

Lithium-ion batteries (LIBs) are currently the dominant energy storage technology for portable and automotive applications; however, the high cost and geographical constraints of lithium resources make it impossible to sustain and meet the exploding market demands.<sup>1</sup> As an alternative to LIBs, sodium-ion batteries (SIBs) are gaining increased recognition as next generation low cost energy storage devices, owing to the natural abundance of sodium resources (~2.5% in the Earth's crust) and their similar electrochemical properties to LIBs.<sup>2,3</sup> A series of high-performance sodium storage electrode materials have been investigated to pursue the ever-growing demand for higher energy density.<sup>4</sup> Cathode materials such as layered oxides,<sup>5</sup> polyanionic compounds,<sup>6,7</sup> and Prussian blue analogues,<sup>8</sup> as well as anode materials such as hard carbons,<sup>9</sup> conversion

materials,<sup>10</sup> and alloy compounds,<sup>11,12</sup> have all demonstrated high specific capacity and excellent cycle stability.

However, the low initial coulombic efficiency (ICE), an intrinsic problem of anode materials, is generally ignored by researchers but seriously impedes the improvement of the energy density of SIBs.<sup>13,14</sup> The low ICE signifies that a large number of active sodium ions are irreversibly consumed to form a solid electrolyte interphase (SEI) layer on the anode during the first cycle.<sup>15</sup> This adverse effect is not as strongly felt in half cells, since the Na metal counter electrode can provide ample Na sources. However, as for Na-ion full cells, where the Na-containing cathode is the only reserve of active sodium ions, such a considerable  $\text{Na}^+$  loss dramatically reduces the overall energy density and shortens the lifespan of full cells. For instance, hard carbon (HC) anodes usually have a low ICE of only 60–80%, which leads to nearly one-third of capacity loss during the initial charge process.<sup>16</sup>

Numerous research efforts have been committed to resolving this issue by offering an additional Na source to counteract the initial capacity loss (ICL) of anodes, known as presodiation.<sup>17,18</sup> In the early stage, presodiation has been carried out by the operation of highly active Na metal. Examples include direct contact of the anode electrodes with Na metal disks<sup>19</sup> or assembling them into a primary cell.<sup>20</sup> In these cases, the irreversible capacity can be readily dismissed *via* the self-discharge

<sup>a</sup>Hubei Key Laboratory of Electrochemical Power Sources, College of Chemistry and Molecular Sciences, Wuhan University, Wuhan, Hubei 430072, China. E-mail: [jfqian@whu.edu.cn](mailto:jfqian@whu.edu.cn)

<sup>b</sup>Hubei Baijierui Advanced Materials Co., Ltd, Wuhan, Hubei 430072, China

<sup>c</sup>College of Chemistry and Molecular Sciences, Wuhan University, Wuhan, Hubei 430072, China

<sup>†</sup> Electronic supplementary information (ESI) available. See DOI: <https://doi.org/10.1039/d3sc03498d>



or electrochemical discharge mechanism. Another effective approach is to incorporate sacrificial sodium salts such as  $\text{NaN}_3$ ,<sup>21</sup>  $\text{Na}_2\text{C}_2\text{O}_4$ ,<sup>22</sup> and  $\text{Na}_2\text{C}_4\text{O}_4$ ,<sup>23</sup> and  $\text{Na}_3\text{C}_6\text{H}_5\text{O}_7$ ,<sup>24</sup> into the cathode side by using their irreversible charging capacity through the electrochemical decomposition mechanism with undesirable impurity generation. Developing a sodium-enriched cathode that can provide extra endogenous sodium ions (beyond its normal stoichiometric ratio) is also an intriguing presodiation method. For instance, the  $\text{Na}_3\text{V}_2(\text{PO}_4)_3$  ( $\text{Na}_3\text{VP}$ ) cathode can safely accommodate over-stoichiometric  $\text{Na}^+$  to form novel Na-enriched materials of  $\text{Na}_4\text{V}_2(\text{PO}_4)_3$  ( $\text{Na}_4\text{VP}$ ) and  $\text{Na}_5\text{V}_2(\text{PO}_4)_3$  ( $\text{Na}_5\text{VP}$ ), which correspond to distinct sodiation plateaus at approximately  $\sim 1.6$  V and  $\sim 0.3$  V *vs.*  $\text{Na}^+/\text{Na}$ , respectively.<sup>25–29</sup> Each excess  $\text{Na}^+$  in the formula theoretically provides an additional  $58.8 \text{ mA h g}^{-1}$  charging capacity. Li *et al.*<sup>27</sup> prepared a  $\text{Na}_4\text{VP}$  electrode by electrochemically discharging  $\text{Na}_3\text{VP}$  to  $1.0$  V *vs.*  $\text{Na}^+/\text{Na}$ . The intermediate product  $\text{Na}_4\text{VP}$  is then used as a cathode and an extra Na source to sodiate hard carbon, after which it reverts to  $\text{Na}_3\text{VP}$  with no residue left in the cell configurations. The resulting  $\text{Na}_4\text{VP}||\text{HC}$  full cell exhibits a high energy density of  $265 \text{ W h kg}^{-1}$ , which is  $76\%$  higher than that of  $151 \text{ W h kg}^{-1}$  for the  $\text{Na}_3\text{VP}||\text{HC}$  control cell. Nevertheless, the electrochemical presodiation procedure is complicated and time-consuming, and thus not suitable for industrial application due to the multiple assembling-disassembling steps.

Alternatively, chemical presodiation using hyperactive arene-sodium reagents is more promising from the perspective of application considering its high efficiency, straightforward operation, and easily scalable feature.<sup>30,31</sup> Many aromatic sodium complexes, such as biphenyl sodium (Biph-Na) and naphthalene sodium (Naph-Na), with redox potentials of  $0.16$  and  $0.09$  V (*vs.*  $\text{Na}^+/\text{Na}$ ), have been widely investigated in presodiation for anode materials.<sup>32–36</sup> Liu and coworkers used Biph-Na as a liquid sodium source and obtained  $\text{Na}_4\text{VP}$  electrodes after immersing  $\text{Na}_3\text{VP}$  for  $30$  s. In anode-free  $\text{Na}_4\text{VP}||\text{Al}$  batteries and  $\text{Na}_4\text{VP}||\text{HC}$  full cells, the efficiency of the presodiation strategy has been reconfirmed with indicators of significantly increased specific capacity and lifespan.<sup>26</sup> However, it should be pointed out that Biph-Na adopted by Liu *et al.* may not be a suitable reagent for  $\text{Na}_4\text{VP}$  generation because of their potential mismatch (which will be discussed in detail below), that might cause oversodiation to form  $\text{Na}_5\text{VP}$ . Besides, a series of parasite reactions including structure degradation and interface damage will be triggered during the over-reduction process, which negatively affect electrochemical performance.<sup>37–39</sup> In conclusion, the key to cathode presodiation is to design sodiation reagents with modest reducing ability that are specifically designed for cathode materials.

Herein, we first developed a phenazine-mediated ambient chemical sodiation strategy to controllably synthesize a Na-enriched  $\text{Na}_4\text{V}_2(\text{PO}_4)_3$  cathode guided by the principle of redox-potential matching. Phenazine-sodium (PNZ-Na) is elaborately screened as the optimal sodiation reagent because it possesses an appropriate reducing potential of  $1.56$  V *vs.*  $\text{Na}^+/\text{Na}$ , which is just below the sodiation potential of  $\text{Na}_3\text{VP}/\text{Na}_4\text{VP}$  ( $1.67$  V *vs.*  $\text{Na}^+/\text{Na}$ ), but much higher than that of the over-

sodiation reaction turning into  $\text{Na}_5\text{VP}$  ( $0.28$  V *vs.*  $\text{Na}^+/\text{Na}$ ). The crystal structure, sodiation reaction mechanism and electrochemical performance of the as-obtained  $\text{Na}_4\text{VP}$  have been verified by multiple characterization techniques, including XRD, XPS, TEM, ssNMR, and electrochemical tests. Benefiting from excess  $\text{Na}^+$  in the formula, the  $\text{Na}_4\text{VP}$  cathode completely compensated the ICL from the anode without any exogenous impurities, resulting in a  $\text{Na}_4\text{VP}||\text{HC}$  full cell exhibiting higher reversible capacity and energy density than the control  $\text{Na}_3\text{VP}||\text{HC}$  full cell.

## Results and discussion

### Screening appropriate sodiation reagents guided by the potential matching principle

$\text{Na}_3\text{V}_2(\text{PO}_4)_3$  with a NASICON (Na super ionic conductor) structure is formed by the corner-sharing of the  $\text{PO}_4$  tetrahedron and  $\text{VO}_6$  octahedron, providing plenty of large channels for  $\text{Na}^+$  diffusion.<sup>40</sup> As depicted in Fig. 1a, its crystal structure contains three isolated sodium storage sites with different oxygen surroundings, namely occupied  $\text{Na}1$  and  $\text{Na}2$  sites and a vacant  $\text{Na}3$  site. More specifically, two  $\text{Na}^+$  ions at the  $\text{Na}2$  site ( $0.67$  occupation) exhibit electrochemical activity, while one  $\text{Na}^+$  ion at the  $\text{Na}1$  site ( $1.0$  occupation) is electrochemically inert. The remaining empty sites enable the lattice to accommodate over-stoichiometric  $\text{Na}^+$  and further generate Na-enriched phases.<sup>41</sup>

As the cathode,  $\text{Na}_3\text{VP}$  undergoes a typical biphasic transition to form  $\text{Na}_4\text{V}_2(\text{PO}_4)_3$  ( $\text{Na}_4\text{VP}$ ) and completely removes two  $\text{Na}^+$  from the  $\text{Na}2$  site accompanied by two  $\text{V}^{3+}$  oxidizing to  $\text{V}^{4+}$ , resulting in a theoretical capacity of  $117.6 \text{ mA h g}^{-1}$  and a voltage plateau at  $3.36$  V *vs.*  $\text{Na}^+/\text{Na}$  (Fig. 1b). Recent investigations revealed that the  $\text{V}^{2+}/\text{V}^{3+}$  redox couple in  $\text{Na}_3\text{VP}$  can also be activated by controlling the sodiation depth, *viz.*, the potential window of charge/discharge measurement.<sup>25</sup> In the over-discharging process (Fig. 1b), two  $\text{V}^{3+}$  in  $\text{Na}_3\text{VP}$  can be reduced to  $\text{V}^{2+}$  respectively and over-stoichiometric  $\text{Na}^+$  is embedded in the lattice to balance the charge. The first  $\text{Na}^+$  is inserted into the empty  $\text{Na}2$  site to generate the  $\text{Na}_4\text{V}_2(\text{PO}_4)_3$  phase ( $\text{Na}_4\text{VP}$ ,  $1.67$  V *vs.*  $\text{Na}^+/\text{Na}$ ), followed by the second  $\text{Na}^+$  in the vacant  $\text{Na}3$  site to generate the  $\text{Na}_5\text{V}_2(\text{PO}_4)_3$  phase ( $\text{Na}_5\text{VP}$ ,  $0.28$  V *vs.*  $\text{Na}^+/\text{Na}$ ). Of particular note, deep-sodiated  $\text{Na}_5\text{VP}$  is energetically unfavorable due to the intense coulombic repulsion, thus leading to an extraordinarily low voltage plateau.

The structure evolution of  $\text{Na}_3\text{VP}$  during the desodiation/sodiation process is intensively investigated by *in situ* XRD (Fig. 1c and S1†). Initially, all diffraction peaks can be assigned to  $\text{Na}_3\text{VP}$ , showing a rhombohedral structure with a space group of  $\text{R}-3\text{c}$ .<sup>25</sup> When charging (desodiation) to  $3.7$  V, the diffraction peaks of  $\text{Na}_3\text{VP}$  diminish gradually while the peaks of  $\text{Na}_4\text{VP}$  increase, presenting continuous phase transformation. The peak shift to higher angles demonstrates lattice shrinkage resulting from the removal of  $\text{Na}^+$ . During the discharge (sodiation) process, an opposite trend is observed from  $\text{Na}_4\text{VP}$  to  $\text{Na}_3\text{VP}$ . Afterwards, over-discharging leads to the appearance of the  $\text{Na}_5\text{VP}$  new phase, as indicated by a plateau at around  $1.67$  V (*vs.*  $\text{Na}^+/\text{Na}$ ) and emerging diffraction peaks at  $23.5^\circ$ ,  $28.5^\circ$ ,  $30.8^\circ$ ,



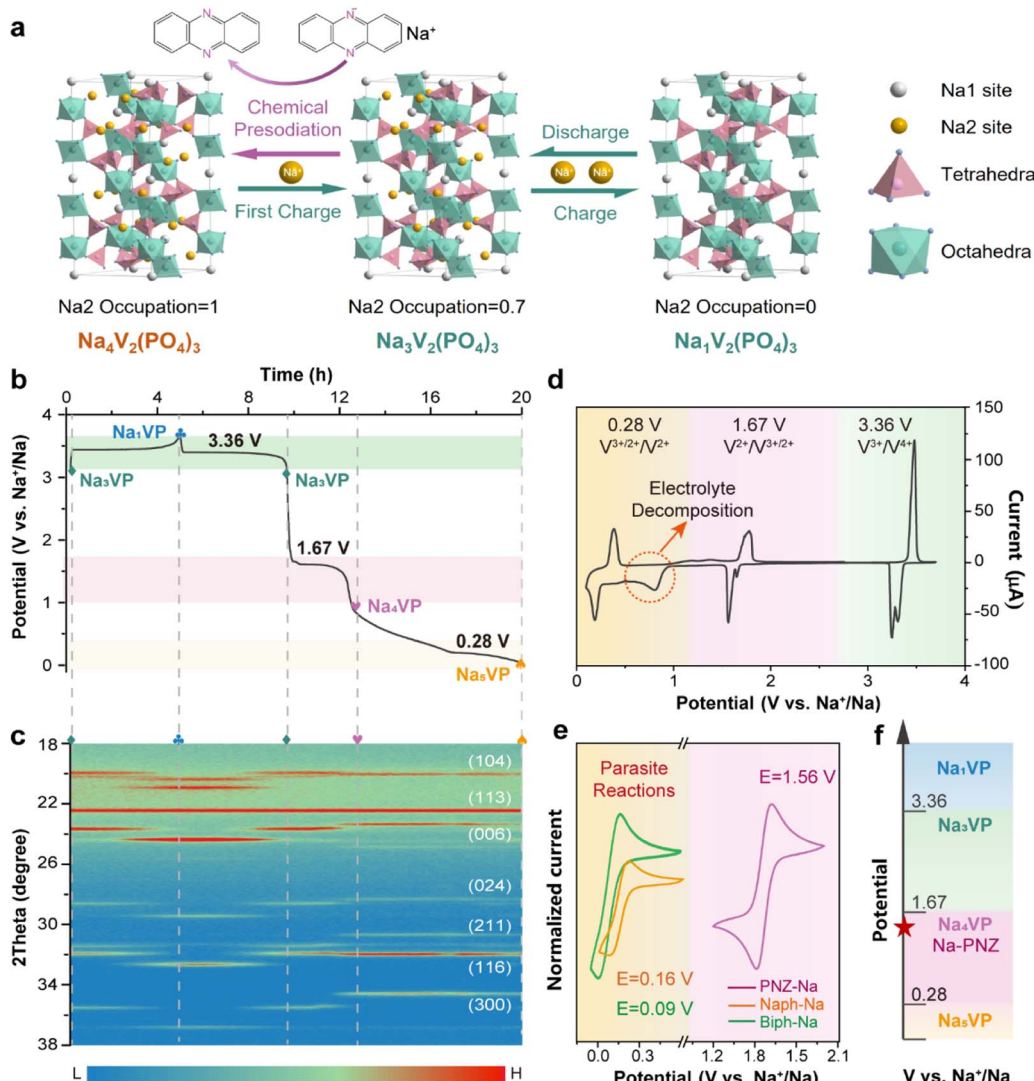


Fig. 1 (a) Schematic illustration of chemical presodiation and the subsequent cycling process of the  $\text{Na}_3\text{VP}$  cathode. (b) Initial charge–discharge profile of  $\text{Na}_3\text{VP}$  and (c) the corresponding *in situ* XRD counter map. (d) Cyclic voltammogram profiles of the  $\text{Na}_3\text{VP}$  cathode in the potential range of 0.1–3.7 V vs.  $\text{Na}^+/\text{Na}$ . (e) Cyclic voltammogram profiles of different sodiation reagents: phenazine-sodium (PNZ-Na), naphthalene-sodium (Nap-Na), and biphenyl-sodium (Biph-Na) at a scan rate of 50 mV s<sup>−1</sup>. (f) Illustration diagram of the potential matching principle for chemical sodiation of  $\text{Na}_3\text{VP}$ .

and 34.7° with gradually increasing intensity, which is in good agreement with previous reports.<sup>27,41</sup> This demonstrates that the two phases coexist and correspond directly to the voltage plateau. Upon further sodiation, a new plateau appears at about 0.28 V (vs.  $\text{Na}^+/\text{Na}$ ) while diffraction peaks at 23.5° and 28.5° fade away gradually, accompanying the formation of  $\text{Na}_5\text{VP}$ .<sup>28</sup> Operando XRD confirms the feasibility of the presodiation strategy to produce sodium-enriched phases from  $\text{Na}_3\text{VP}$  and reveal the corresponding structure information.

The cyclic voltammogram (CV) profile (Fig. 1d) obtained between 0.1 and 3.7 V (vs.  $\text{Na}^+/\text{Na}$ ) reconfirms the accessibility of  $\text{Na}_4\text{VP}$  and  $\text{Na}_5\text{VP}$ . Three pairs of cathodic/anodic peaks located at ~0.20/0.36, ~1.56/1.78 and ~3.30/3.48 V are in good agreement with plateaus observed in the galvanostatic charge/discharge profiles (eqn (1)–(3)). Notably, a broad irreversible peak is observed between 0.3 and 0.9 V, implying aggressive

electrolyte decomposition. During the cycles (Fig. S2†), all the peak currents prominently diminish and the polarization gradually increases, owing to the structure deterioration of active materials and the accumulation of the SEI on the electrode surface. In contrast, the CV curves between 1.0 and 4.0 V almost completely overlapped after the initial cycle (Fig. S3†), indicating the highly reversible phase transition among  $\text{Na}_1\text{VP}$ ,  $\text{Na}_3\text{VP}$ , and  $\text{Na}_4\text{VP}$ . The split of the cathodic peak in the first cycle may be ascribed to the minor structure rearrangement of the active material.<sup>42</sup> The narrower CV peaks also imply a faster  $\text{Na}^+$  insertion process for  $\text{Na}_4\text{VP}$  than  $\text{Na}_5\text{VP}$ . It is important to note that  $\text{Na}_5\text{VP}$  exhibits low initial coulombic efficiency (ICE<sub>cathode</sub> is defined as the ratio of sodiation capacity to desodiation capacity of a cathode), rendering it incompatible with HC anodes (Fig. S4†). As mentioned above, the typical ICE<sub>anode</sub> (defined as the ratio of desodiation capacity to sodiation

capacity of an anode) of HC anodes is only 60–80%. When  $\text{Na}_5\text{VP}$  with an ICE of merely 40% matches with HC anodes, surplus  $\text{Na}^+$  will be introduced into the full cells and form uncontrollable sodium dendrites on the anode side, resulting in safety concerns. Therefore,  $\text{Na}_4\text{VP}$  has a suitable ICE ( $\sim 64\%$ ) and excellent structural stability, denoting its superiority for active sodium compensation in full cells.

As displayed in Fig. 1e, currently reported aromatic sodium reagents, such as Biph-Na and Naph-Na, demonstrate ultra-low redox potentials of 0.16 V and 0.09 V *vs.*  $\text{Na}^+/\text{Na}$  for cathode materials (lower than the  $\text{Na}_5\text{VP}$  formation potential of 0.28 V *vs.*  $\text{Na}^+/\text{Na}$ ). In order to prevent over-sodiation from yielding  $\text{Na}_5\text{VP}$  or other parasite reactions, the treatment duration with sodium reagents must be strictly controlled, which is not conducive to industrial batch application. Therefore, it is of utmost importance to develop appropriate sodium reagents to achieve a refined precise and controllable preparation of  $\text{Na}_4\text{VP}$ .

$\text{Na}^+$  insertion/extraction reaction of  $\text{Na}_x\text{VP}$ :



Preparation of the PNZ-Na reagent:



Precise chemical sodiation of  $\text{Na}_3\text{VP}$  enabled by the PNZ-Na reagent:



In accordance with the potential-matched chemical sodiation strategy (Fig. 1f), phenazine sodium (PNZ-Na) has been elaborately chosen as a suitable sodiation reagent due to its appropriate potential. The PNZ-Na reagent displays a pair of reversible redox peaks at 1.51 and 1.62 V (*vs.*  $\text{Na}^+/\text{Na}$ , Fig. 1e), corresponding to the PNZ/PNZ<sup>−</sup> redox couple (eqn (4)). PNZ-Na exhibits the highest potential as a sodiation reagent reported so far,<sup>26,32,33,43</sup> benefiting from the strong electron-withdrawing effect of nitrogen atoms and the efficient charge dispersion provided by the additional six-membered ring.<sup>44,45</sup> Hence, the end-point of the reaction is effectively clamped by the PNZ-Na reagent potential, thus preventing over-sodiation. During the chemical presodiation process, reductive PNZ-Na concurrently donates  $\text{Na}^+$  and  $\text{e}^-$  for  $\text{Na}_3\text{VP}$  while also leading to the recovery of intrinsic phenazine molecules (eqn (5)). The sodium ions diffuse into the  $\text{Na}_3\text{VP}$  lattice and locate at the partially occupied  $\text{Na}_2$  site to form a pure  $\text{Na}_4\text{VP}$  phase.

### Controllable synthesis of Na-enriched $\text{Na}_4\text{VP}$ *via* the chemical sodiation strategy

The chemical presodiation of the  $\text{Na}_3\text{VP}$  cathode is conducted simply by immersing the electrode into PNZ-Na solution for a particular time, followed by DME rinse to remove the residual

PNZ-Na. Phenazine and sodium metal are mixed in dimethoxyethane (DME) solvent in equal amounts to obtain the PNZ-Na reagent, as described in eqn (4). The strong electron affinity of heterocyclic aromatics causes the outermost electrons of Na metal to transfer spontaneously to the conjugated phenazine rings, producing grape-purple colored PNZ<sup>−</sup> radicals (Fig. 2a left).<sup>46,47</sup> Once the  $\text{Na}_3\text{VP}$  electrode is immersed in the PNZ-Na solution, the sodiation reaction proceeds through electron transfer from the PNZ<sup>−</sup> radical to  $\text{Na}_3\text{VP}$  along with  $\text{Na}^+$  accommodation to form  $\text{Na}_4\text{VP}$  (eqn (5)). Following the reaction, the purple PNZ<sup>−</sup> radical dissolved in DME is converted to a pristine PNZ molecule, resulting in the PNZ-Na solution fading (Fig. 2a right).

To probe the reaction pathways, we prepared presodiated  $\text{Na}_x\text{VP}$  ( $3 \leq x \leq 4$ ) electrodes with various immersion times of 30–120 s. As the reaction time increases, the emergence of new diffraction peaks at 30.8° and 34.7°, along with growing intensity, is attributable to the  $\text{Na}_4\text{VP}$  phase, while the peaks of  $\text{Na}_3\text{VP}$  at 31.6° (116) and 35.6° (300) weaken (Fig. 2b). This outcome reveals that two phases,  $\text{Na}_3\text{VP}$  and  $\text{Na}_4\text{VP}$ , coexist during the presodiation process (30 s and 60 s), which is consistent with *in situ* XRD and prior reports.<sup>26,28</sup> Notably,  $\text{Na}_3\text{VP}$  is completely converted to  $\text{Na}_4\text{VP}$  after presodiation for more than 90 s. (Fig. S5†) The XRD pattern of chemically presodiated  $\text{Na}_4\text{VP}$  is identical to that of electrochemically sodiated  $\text{Na}_4\text{VP}$ , implying a rapid  $\text{Na}^+$  migration in the cathode and a uniform sodiation process achieved by chemical presodiation. The inductively coupled plasma atomic emission spectroscopy (ICP-OES) tests accurately determine the Na content in different samples (Fig. 2c). The samples with treatment time of 30, 60, and over 90 s are accordingly denoted as  $\text{Na}_{3.37}\text{VP}$ ,  $\text{Na}_{3.68}\text{VP}$ , and  $\text{Na}_4\text{VP}$ .

The presodiation degree of  $\text{Na}_x\text{VP}$  achieved *via* chemical treatment is also evaluated using electrochemical performance in sodium half-coin cells. The initial charge curves of  $\text{Na}_x\text{VP}$ , including ICE and plateau capacity at about 1.67 V that correspond to  $\text{Na}_4\text{VP}$ , are displayed in Fig. 2d and e. The open circuit voltage (OCV *vs.*  $\text{Na}^+/\text{Na}$ ) dramatically drops during the biphasic process from  $\text{Na}_3\text{VP}$  to  $\text{Na}_4\text{VP}$ , after which it remains stable at around 1.67 V. The presodiated  $\text{Na}_x\text{VP}$  exhibits a continuous increase in initial charge capacity (*i.e.*, Na extraction), whereas the ICE decreases with increasing sodiation time, indicating a sustained  $\text{Na}^+$  insertion reaction (Fig. S6†). Consequently, the chemical presodiation process continues until  $\text{Na}_3\text{VP}$  diminishes, as reflected by a constant ICE of  $\sim 64\%$  and an increased specific capacity of  $\sim 56 \text{ mA h g}^{-1}$ , respectively. Notably, no unnecessary parasitic reactions are introduced due to the identical charge-discharge curves and ICE between chemical and electrochemical sodiation (Fig. S7a†). The redox potentials between the reductive agent and  $\text{Na}_3\text{VP}$  are well-matched, thereby avoiding the issues of over-sodiation, inhomogeneity, and inconsistency during scaling up for mass production. Even with excessive treatment time (30 min) and reagent dosage, there is no structural damage to the cathode materials, demonstrating the success of our chemical presodiation strategy based on the redox-potential matched principle (Fig. S7b†). The sodiation reaction self-terminates once all



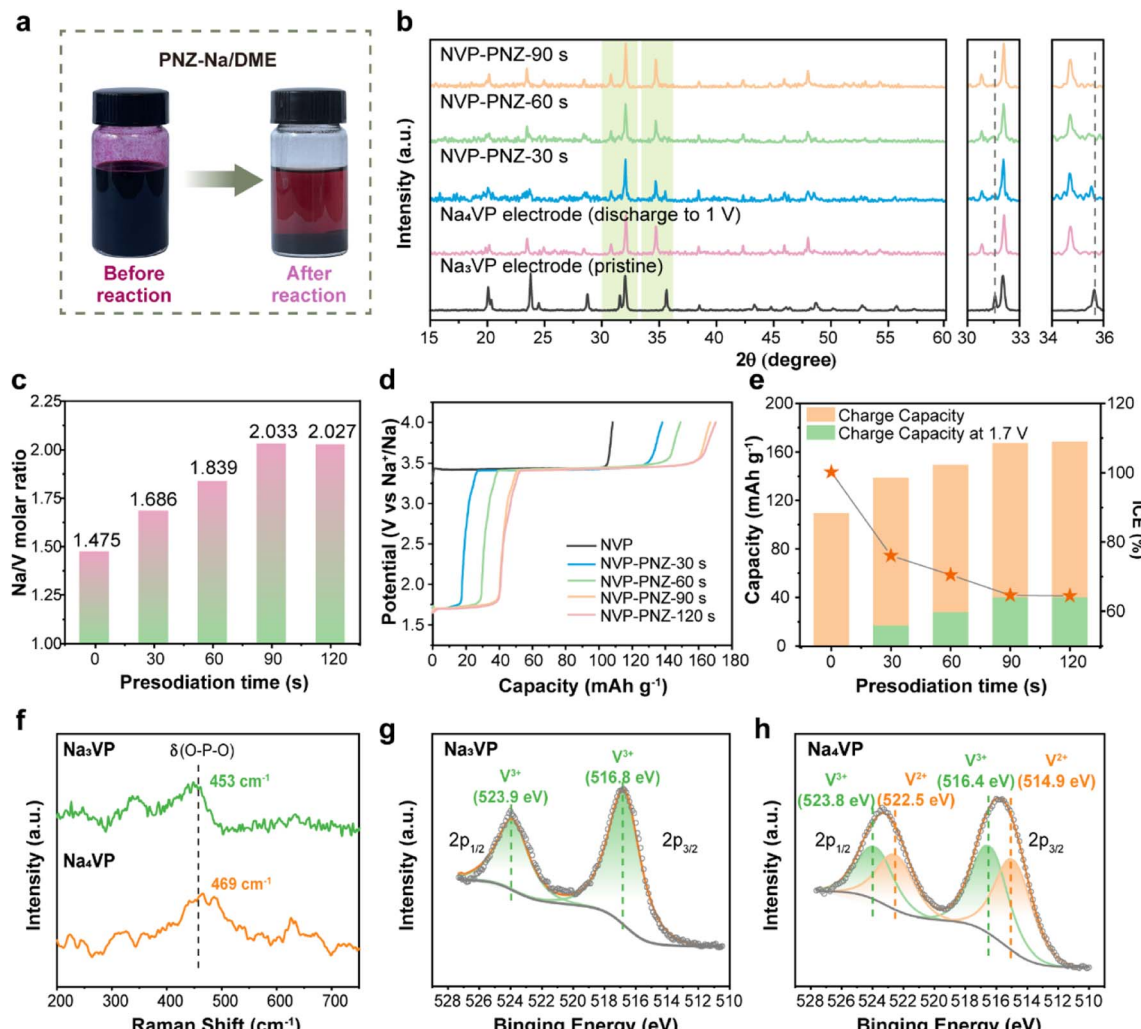


Fig. 2 (a) Optical photographs of the phenazine sodium reagent before and after reaction with  $\text{Na}_3\text{VP}$ . (b) XRD patterns, (c) ICP results, (d) initial charge curve, and (e) initial charge capacity and ICE of the  $\text{Na}_3\text{VP}$  electrodes with different presodiation times. (f) Raman spectroscopy spectra of  $\text{Na}_3\text{VP}$  and  $\text{Na}_4\text{VP}$ . XPS V 2p spectra of (g)  $\text{Na}_3\text{VP}$  and (h)  $\text{Na}_4\text{VP}$ .

$\text{Na}_3\text{VP}$  transforms into sodium-rich  $\text{Na}_4\text{VP}$  due to the elaborately screened sodiation reagents. We further conducted the *in situ* XRD test of the PNZ-Na presodiated  $\text{Na}_4\text{VP}$  electrode (Fig. S8 and S9<sup>†</sup>). The variation of diffraction peaks is consistent with the electrochemical sodiation process, and there is no impurity phase introduced by presodiation treatment. It is a highly reversible transformation between  $\text{Na}_4\text{VP}$  and  $\text{Na}_3\text{VP}$  and reconfirms that presodiation has no adverse effect on the lattice structure. Therefore, the reliability of the chemical presodiation strategy is firmly authenticated.

Raman spectra and X-ray photoelectron spectroscopy (XPS) are further employed in order to explore the effect of presodiation treatment on the structure of the  $\text{Na}_3\text{VP}$  cathode. The Raman spectra shown in Fig. 2f indicate that the symmetric bending vibration peak of the  $\text{PO}_4$  tetrahedron in  $\text{Na}_3\text{VP}$  at  $453\text{ cm}^{-1}$  is slightly blue-shifted after presodiation treatment. This result suggests the enhancement of P–O bond energy and boosting ionicity of the  $\text{Na}_4\text{VP}$  lattice.<sup>48</sup> The valence states of vanadium ions are verified by the XPS results. The survey XPS

spectrum (Fig. S10<sup>†</sup>) confirms the presence of the same chemical composition elements in  $\text{Na}_3\text{VP}$  and  $\text{Na}_4\text{VP}$ . The binding energy of P 2p shifts toward the higher energy direction (from 133.4 eV to 133.7 eV), reconfirming the stronger P–O bonds (Fig. S11<sup>†</sup>). As seen in Fig. 2g and h, the V 2p peaks broaden after presodiation and reveal the coexistence of mixed  $\text{V}^{3+}$  and  $\text{V}^{2+}$  ions in the lattice. The two peaks of  $\text{Na}_3\text{VP}$  at 516.8 eV and 523.9 eV coincide with  $\text{V} 2p_{3/2}$  and  $\text{V} 2p_{1/2}$  of  $\text{V}^{3+}$ , which means only trivalent vanadium is observed in the pristine electrode.<sup>49</sup> Except for the peaks above, new peaks at 514.9 eV and 522.5 eV can be ascribed to the contribution of  $\text{V}^{2+}$  in  $\text{Na}_4\text{VP}$ .<sup>26</sup> Further quantitative analysis of the V 2p spectrum indicates a  $\text{V}^{3+}/\text{V}^{2+}$  ratio of 0.49/0.51 based on the integral area of deconvoluted peaks, which agrees well with the valence distribution for  $\text{Na}_4\text{VP}$ . All the characterization studies above demonstrate that the PNZ-Na solution can readily and controllably presodiate the  $\text{Na}_3\text{VP}$  cathode in a relatively short time.

The morphological evolution of the  $\text{Na}_3\text{VP}$  and  $\text{Na}_4\text{VP}$  samples is investigated by scanning electron microscopy (SEM),

focused ion beam (FIB), and high-resolution transmission electron microscopy (HRTEM). The results show that both  $\text{Na}_3\text{VP}$  and  $\text{Na}_4\text{VP}$  exhibit a regular spherical morphology, with a diameter ranging from 5–15  $\mu\text{m}$ , consisting of primary particles that are densely packed to form secondary particles (Fig. 3a and d). Apparently, the morphology characteristic of sodiated  $\text{Na}_4\text{VP}$  is not affected by the chemical treatment and helps to retain the electrochemical performance (Fig. S12†). The energy-dispersive X-ray (EDX) analysis reconfirms the Na/V ratios of  $\text{Na}_3\text{VP}$  and  $\text{Na}_4\text{VP}$  to be 1.49 and 1.99, respectively (Fig. S13†). Cross sections are obtained by FIB-SEM to monitor microstructural damage, while no microcracks are observed after presodiation treatment (Fig. 3b and e). It should be noted that the internal voids in the particles are formed by primary particle agglomeration rather than structure degradation. HRTEM images in Fig. 3c reveal well-defined lattice fringes of 0.373 nm ascribed to the (113) planes in the  $\text{Na}_3\text{VP}$  lattice. Likewise, we observe characteristic lattice fringes of 0.378 nm (Fig. 3f), corresponding to the emerging 23.5° diffraction peak in the  $\text{Na}_4\text{VP}$  lattice (Fig. 2b).

$^{23}\text{Na}/^{31}\text{P}$  solid state nuclear magnetic resonance (ssNMR) offers in-depth insights into local structural transformation while probing the oxidation states of the neighboring vanadium ions. For  $^{31}\text{P}$  spectra, the signals are caused by the unpaired electronic spin transfer from TM d orbitals to the  $^{31}\text{P}$  nuclei through chemical bonds.<sup>50</sup> Fig. S14† presents the room temperature  $^{31}\text{P}$  spectra for  $\text{Na}_3\text{VP}$  and  $\text{Na}_4\text{VP}$ . In the  $\text{Na}_3\text{VP}$  lattice, a broad asymmetric peak at 2000–3500 ppm reflects a twisted environment for the  $^{31}\text{P}$  nuclei.<sup>51</sup> While in  $\text{Na}_4\text{VP}$ , the corresponding peak with decreasing intensity reveals the reducing dipolar interaction between unpaired electron spins of V and P nuclei. In contrast, a new broad peak at 3500–5000 ppm is observed in  $\text{Na}_4\text{VP}$ , which is attributed to the

complicated interaction between  $\text{V}^{2+}$  and adjacent phosphate groups.<sup>50</sup> This phenomenon is because the  $\text{V}^{2+}$  ( $t_{2g}^3 e_g^0$ ) owning three unpaired electrons is more paramagnetic than  $\text{V}^{3+}$  ( $t_{2g}^2 e_g^0$ ) and generally causes a larger Fermi contact shift. Similar results are also observed in  $^{23}\text{Na}$  spectra.

Turning to the  $^{23}\text{Na}$  NMR spectra, the signals of  $\text{Na}_4\text{VP}$  are recorded at 8, 10, and 12 kHz to distinguish the isotropic signals and spinning side bands denoted by asterisks (Fig. 4a). A typical  $^{23}\text{Na}$  spectrum of  $\text{Na}_3\text{VP}$  is presented in Fig. 4b and c, which includes two significant signals at 83 and 18 ppm with very different magnitudes and a set of spinning side bands. As previously reported by Hu *et al.*,<sup>52</sup> the oxidation state of vanadium centers coordinated with Na at Na1 sites is higher than those coordinated with Na at Na2 sites, leading to a more significant  $^{23}\text{Na}$  shift at the Na2 site in contrast with that at the Na1 site. Similar paramagnetic effects have also been reported in LIBs on  $^7\text{Li}$  NMR shifts.<sup>53</sup> Based on these results, the signals at 83 and 18 ppm are assigned to the partially occupied Na2 site and fully filled Na1 site, respectively. Only Na at the Na2 site has electrochemical activity on account of the relatively weak bonding. The signal peaks shrink and slightly shift to the higher direction with the increasing sodium content of these samples (Fig. 4b). This phenomenon suggests a more ordered environment of Na, whereas more  $\text{V}^{2+}$  leads to a higher shift. We speculate that the shrinkage of peaks from  $\text{Na}_3\text{VP}$  to  $\text{Na}_4\text{VP}$  is due to a decrease in  $\text{Na}^+$  motion. Because of the partially occupied Na2 site,  $\text{Na}_3\text{VP}$  has more Na vacancies than the fully occupied  $\text{Na}_4\text{VP}$ . We further investigate  $\text{Na}^+$  diffusion kinetics by the CV technique at varied scan rates (Fig. S15 and S16†). The  $\text{Na}^+$  diffusion coefficients of  $\text{Na}_4\text{VP}$  decrease as we suspected, indicating the reduced mobility of sodium ions. The fitted spectra of samples with different sodiated degrees are presented in Fig. 4c and d and we conclude that the Na2/Na1 peak

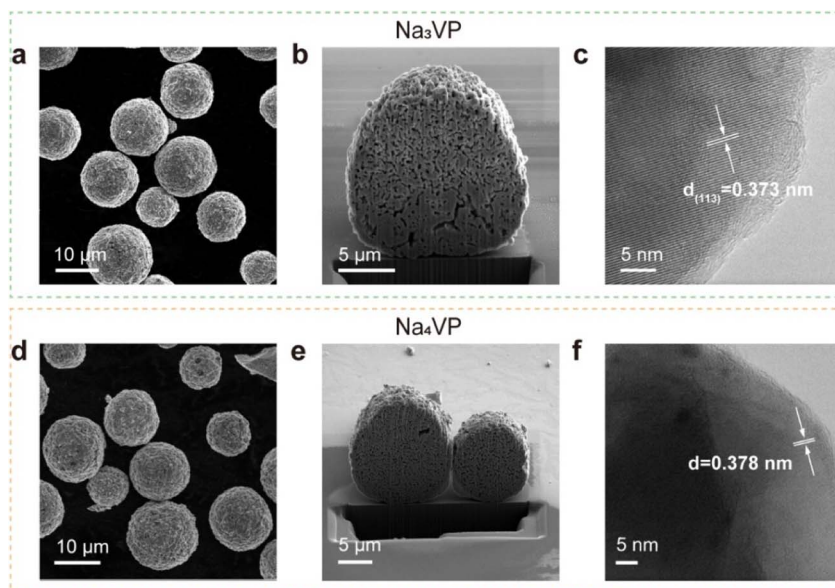


Fig. 3 (a–c) SEM image, cross section and HR-TEM image of  $\text{Na}_3\text{VP}$ , respectively. (d–f) SEM image, cross section and HR-TEM image of  $\text{Na}_4\text{VP}$ , respectively.



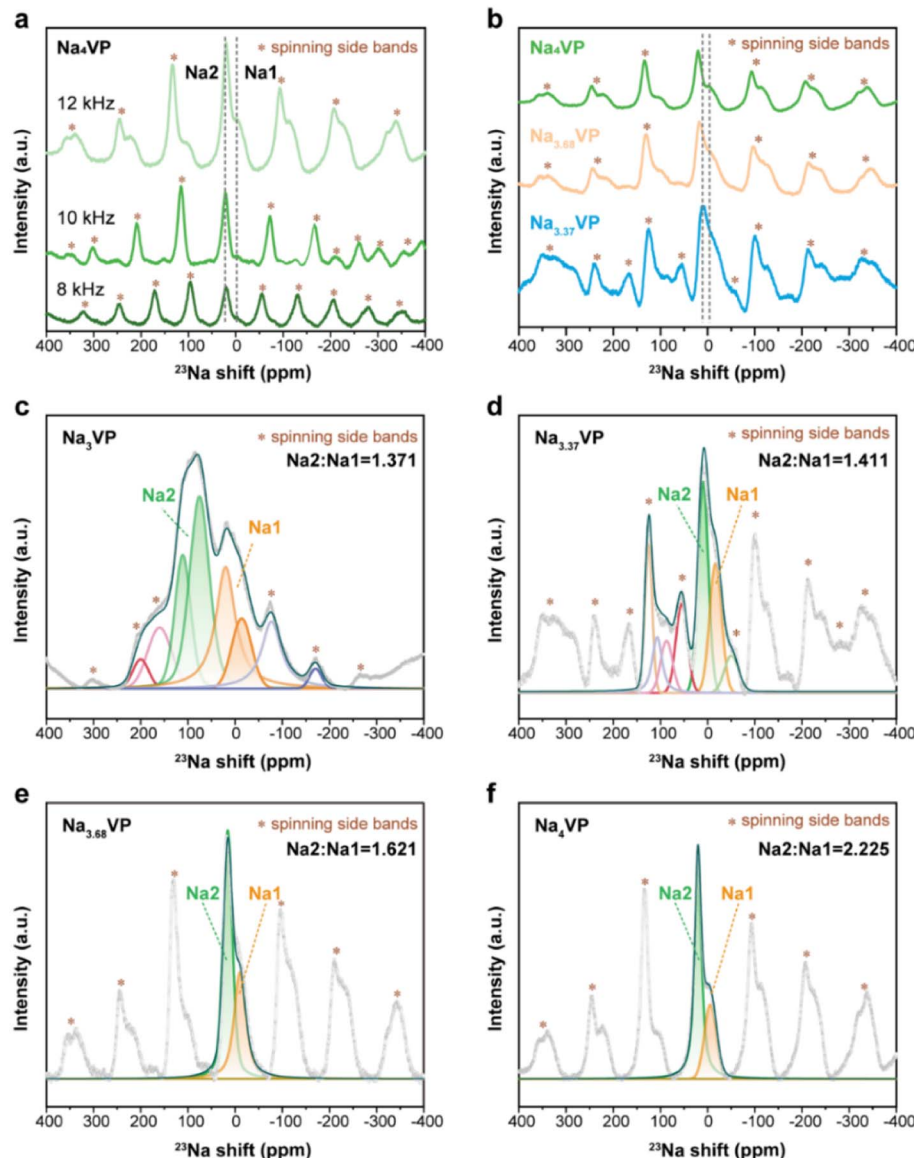


Fig. 4 (a)  $^{23}\text{Na}$  ssNMR spectra of  $\text{Na}_4\text{VP}$  at 8, 10, and 12 kHz. (b)  $^{23}\text{Na}$  ssNMR spectra of  $\text{Na}_x\text{VP}$  with different sodiation depths at 12 kHz. The fitted  $^{23}\text{Na}$  ssNMR spectra of (c)  $\text{Na}_3\text{VP}$ , (d)  $\text{Na}_{3.37}\text{VP}$ , (e)  $\text{Na}_{3.68}\text{VP}$ , and (f)  $\text{Na}_4\text{VP}$ .

area ratio gradually increases from 1.371 to 2.225. In other words, excess sodium ions that  $\text{Na}_3\text{VP}$  receives from the PNZ-Na solution are preferentially accommodated in the  $\text{Na}_2$  site, making it close to completely occupied in the  $\text{Na}_4\text{VP}$  sample.

#### The electrochemical performance of the Na-enriched $\text{Na}_4\text{VP}$ cathode

The sodium storage capability of the sodiated samples is investigated through galvanostatic charge–discharge tests in half-cells with a Na-metal anode. All of the  $\text{Na}_x\text{VP}$  electrodes with different treatment times manifest the same cycling stability at 0.5C for 100 cycles as pristine  $\text{Na}_3\text{VP}$  (Fig. S17†). Even extending the treatment time to 30 min, no discernible capacity decay is observed, suggesting that the electrochemical performance is completely retained after presodiation treatment. Our

presodiation strategy is not strict with processing time and is expected to achieve large-scale production. In the following discussion, we primarily focus on the comparison between pristine  $\text{Na}_3\text{VP}$  and the sodiated  $\text{Na}_4\text{VP}$ . Fig. 5a displays the CV curves of  $\text{Na}_4\text{VP}$  at a scan rate of  $0.1 \text{ mV s}^{-1}$ . The OCV of the  $\text{Na}_4\text{VP}$  sample is close to 1.6 V which is related to the average valence of V ions, in line with previous discussion. During the first cathodic scan, the first oxidation peak appears at around 1.7 V corresponding to the first distinct plateau in the charge profile of  $\text{Na}_4\text{VP}$  (Fig. 5b). These features, which are absent in  $\text{Na}_3\text{VP}$  electrodes, are because of the oxidation  $\text{V}^{2+}/\text{V}^{3+}$  in the Na-enriched phase and the extraction of the pre-doped sodium ions. When all pre-doped sodium is removed, the Na-enriched  $\text{Na}_4\text{VP}$  entirely transforms into  $\text{Na}_3\text{VP}$  and then presents a typical voltage plateau of 3.4 V attributed to the reversible  $\text{V}^{3+}/\text{V}^{4+}$  redox couple, validated by well-overlapped CV profiles. In



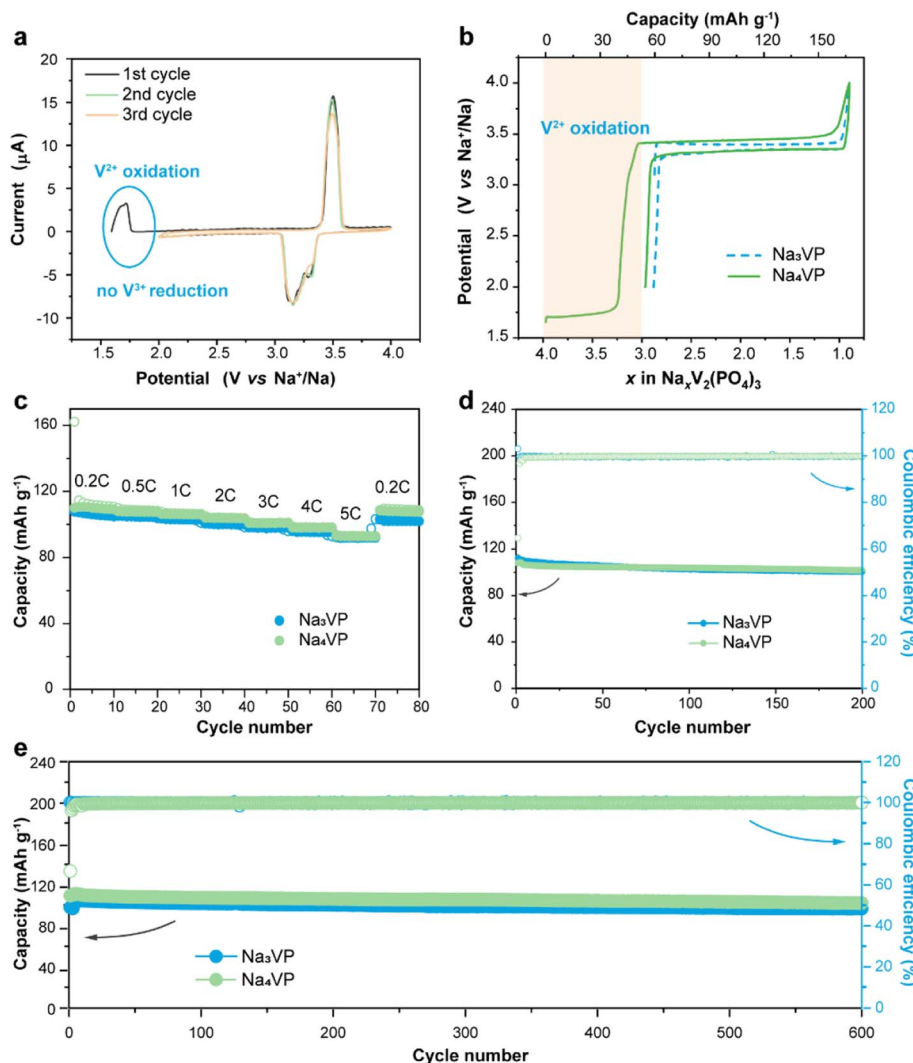


Fig. 5 (a) Cyclic voltammogram profiles of the Na<sub>4</sub>VP cathode at a scan rate of 0.1 mV s<sup>-1</sup>. (b) Initial charge–discharge curves of Na<sub>3</sub>VP and Na<sub>4</sub>VP electrodes between 2.0 and 4.0 V at 0.2C. (c) Rate performance, (d) cycling stability at 0.5C, and (e) long-term cycling stability at 1C of Na<sub>3</sub>VP and Na<sub>4</sub>VP electrodes.

brief, active sodium compensation during cycling is achieved by the irreversible oxidation of V<sup>2+</sup>, *viz.*, by controlling the voltage window. These results reconfirm that the preparation of the Na<sub>4</sub>VP cathode to offer charge compensation and an additional Na reservoir has been successfully implemented. The rate capability and long-term cycling stability of the two samples are analysed as shown in Fig. 5c–e in a voltage window of 2.0–4.0 V (vs. Na<sup>+</sup>/Na). The Na<sub>4</sub>VP electrode exhibits reversible desodiation capacities of 109.4, 107.5, 106.1, 101, 98.1, and 92.8 mA h g<sup>-1</sup> at rates of 0.2, 0.5, 1, 2, 3, 4, and 5C, respectively, slightly higher than that of the Na<sub>3</sub>VP electrode. When the rate comes back to 0.2C, a reversible capacity of about 108 mA h g<sup>-1</sup> is achieved, suggesting the excellent reversibility of the Na<sub>4</sub>VP electrode. The Na<sub>4</sub>VP electrode also retains an outperformed cycling stability with high capacity retentions of 95.3% at 0.5C after 200 cycles and 91.8% at 1C after 600 cycles.

Na<sub>4</sub>VP||HC full cells are assembled to demonstrate the application feasibility of Na<sub>4</sub>VP as both the cathode and extra

Na reservoir in enhancing the energy density of SIBs, and a control cell Na<sub>3</sub>VP||HC is also constructed for comparison. For the fabrication of full cells, the mass matching between the cathode and anode is based on their capacity balance, which is determined by the charge capacity of the cathode and the discharge capacity of the anode. As displayed in Fig. 6a and b, during the first charge, both the irreversible sodium storage sites of the anode and the formation of the SEI will consume considerable active sodium. More Na<sub>3</sub>VP cathode is commonly to be matched with HC and in a Na-poor state in the following cycles, namely Na<sub>3-x</sub>VP. As an alternative, the Na<sub>4</sub>VP electrode used for full cells enables a 35.2 wt% reduction in cathode mass compared to the Na<sub>3</sub>VP electrode and ensures that the cathode as Na<sub>3</sub>VP without Na loss participates in subsequent cycles.

As shown in Fig. 6c, the Na<sub>3</sub>VP||HC and Na<sub>4</sub>VP||HC full cells deliver a charge capacity of 111 and 168 mA h g<sup>-1</sup>, respectively, matching well with the values in half cell configuration. However, the reversible discharge capacity of the Na<sub>3</sub>VP||HC full

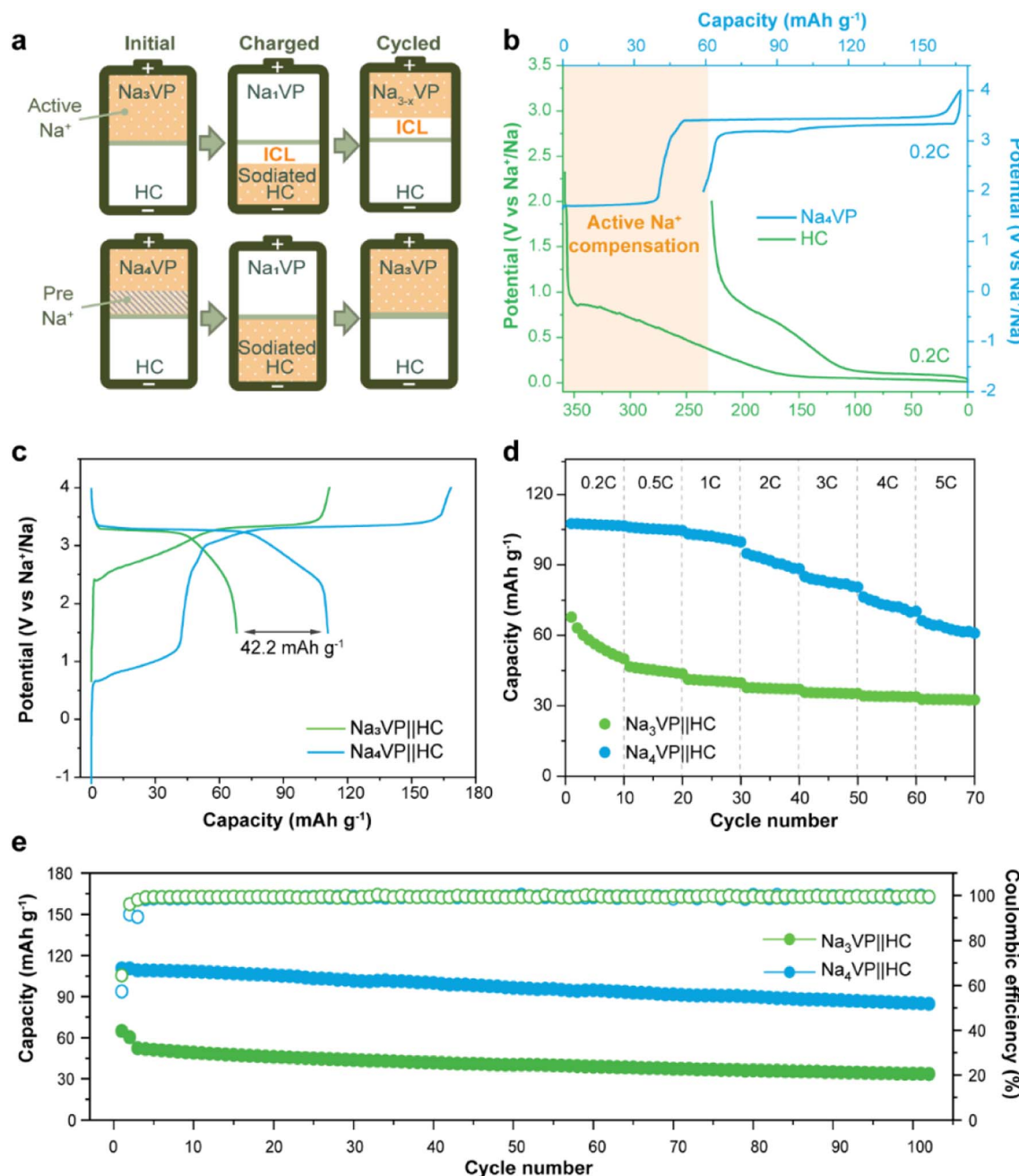


Fig. 6 (a) Schematic illustration of the presodiation process by the Na-enriched Na<sub>4</sub>VP cathode in full cells. (b) Half-cell voltage profiles of the Na<sub>4</sub>VP cathode and the HC anode at 0.2C. (c) Initial voltage profiles, (d) rate performance, and (e) cycling stability at 1C of Na<sub>3</sub>VP||HC and Na<sub>4</sub>VP||HC full cells.

cell is merely 66.6 mA h g<sup>-1</sup> with 39.3% capacity loss. This result can be attributed to the failed Na<sup>+</sup> reinsertion on the cathode side in the absence of extra endogenous Na<sup>+</sup>. In comparison, the full cell with the Na<sub>4</sub>VP cathode shows an initial discharge capacity of 109.7 mA h g<sup>-1</sup> and an ICE of 65%, which are equivalent to that of the Na<sub>3</sub>VP half-cell, demonstrating extremely high utilization of active materials. Similar to other published results (Table S1†), the low ICE is ascribed to irreversible Na compensation during the initial charge cycle, but subsequent average coulombic efficiency is higher than that of

Na<sub>3</sub>VP||HC without presodiation (Fig. S18†). The Na<sub>4</sub>VP||HC full cell shows comparable cycling stability with the control Na<sub>3</sub>VP||HC full cell, but shows markedly enhanced reversible capacity and excellent rate capability (Fig. 6d, e and S19). Fig. 6d demonstrates the rate capability of both Na<sub>4</sub>VP||HC and Na<sub>3</sub>VP||HC full cells from 0.2C to 5C. Na<sub>4</sub>VP||HC displays a respectable rate performance benefiting from the presodated Na<sub>4</sub>VP cathode. Discharge capacities of 107.5, 106, 103.2, 94.8, 84.9, 76.3, and 66.3 mA h g<sup>-1</sup> are delivered at current densities of 0.2, 0.5, 1, 2, 3, 4, and 5C, respectively. Even at a current

density of 5C, corresponding to a charging duration as short as 12 min,  $\text{Na}_4\text{VP}||\text{HC}$  still delivers 61.7% capacity retention of the discharge capacity at 0.2C. In contrast,  $\text{Na}_3\text{VP}||\text{HC}$  exhibits much lower reversible capacity due to active sodium loss. Overall,  $\text{Na}_4\text{VP}||\text{HC}$  exhibits an impressive discharge capacity of  $111 \text{ mA h g}^{-1}$  with an ICE of 66%, and an energy density of  $251.1 \text{ W h kg}^{-1}$  based on the total mass of cathode and anode active materials. This is far superior to those of the control cell using the pristine  $\text{Na}_3\text{VP}$  cathode (ICE of 60% and an energy density of  $159.4 \text{ W h kg}^{-1}$ ). The  $\text{Na}_4\text{VP}||\text{HC}$  full cell shows a decent cycling stability of 78% capacity retention at 1C after 100 cycles and 57% capacity retention at 2C after 500 cycles (Fig. 6e and S19), which is comparable with that of the control  $\text{Na}_3\text{VP}||\text{HC}$  full cell, but shows markedly enhanced reversible capacity. Table S1 in the ESI<sup>†</sup> compares the recently published NVP-based full cells in terms of electrochemical performance and energy density. To the best of our knowledge, the energy density of PNZ-Na presodiated  $\text{Na}_4\text{VP}||\text{HC}$  is among the best of the reported values for NVP-based full cells. These discrepancies strongly suggest that our presodiation strategy can improve the overall energy density of SIBs while simultaneously maintaining decent cycling stability.

## Conclusions

In summary, we have reported a facile and effective chemical presodiation approach to prepare a Na-enriched  $\text{Na}_4\text{VP}$  cathode under the guidance of the redox-potential-matching principle. The phenazine-Na reagent with a redox potential of 1.56 V vs.  $\text{Na}^+/\text{Na}$  was employed to pre-dope active  $\text{Na}^+$  into the  $\text{Na}_3\text{VP}$  lattice for the  $\text{Na}_4\text{VP}$  cathode, successfully retaining the structure stability and electrochemical performance.  $\text{Na}_4\text{VP}$  initially serves as an excess Na reservoir and a cathode to eliminate the active  $\text{Na}^+$  loss on the anode side, allowing the full capacity of  $\text{Na}_3\text{VP}$  to be used for the subsequent cycles. Our presodiation strategy not only enables rapid preparation of  $\text{Na}_4\text{VP}$  and is expected to achieve batch production, but also doesn't bring about any external impurities after sodium compensation. The energy density of the  $\text{Na}_4\text{VP}||\text{HC}$  full cell is  $251.1 \text{ W h kg}^{-1}$ , much greater than that of the  $\text{Na}_3\text{VP}||\text{HC}$  full cell ( $159.4 \text{ W h kg}^{-1}$ ). Most importantly, this approach can be broadly applicable to different cathode materials and opens up new avenues for the design of high-energy SIBs.

## Experimental section

### Materials synthesis

All the reagents were used as received without further treatment. Commercial  $\text{Na}_3\text{VP}$  and hard carbon (BHC400) powders were purchased from Guangdong Canrd New Energy Technology Co., Ltd. Phenazine, biphenyl, naphthalene and electron-grade N-methyl-2-pyrrolidone (NMP) were obtained from Aladdin Chem. Co., Ltd. Anhydrous DME was purchased from JK Chemical. The phenazine-sodium (PNZ-Na) reagent was prepared by adding equal stoichiometric sodium metal and phenazine in DME and stirring for four hours in a glove box. Sodium-enriched  $\text{Na}_4\text{VP}$  was synthesized simply by immersing the  $\text{Na}_3\text{VP}$  powders or cathode

sheet in 0.05 M PNZ-Na solution for a certain time (0–120 s) and then rinsing it with DME to quench the reaction and remove the residue, followed by vacuum drying for 15 min.

### Characterization

XRD patterns were collected on an X-ray diffractometer (Rigaku Smartlab SE) with Cu-K $\alpha$  radiation at 40 kV. *In situ* XRD was performed on a live charge/discharge process to monitor the structure evolution of  $\text{Na}_3\text{VP}$ . Every single pattern was collected for 7 min in the scan range of 18–38°. The morphologies and fine phase structure of samples were obtained by SEM (SEM, Zeiss Merlin Compact) and HRTEM (JEM-2100). The valent information was obtained by XPS (ESCALAB250Xi) with Al Ka radiation. Raman spectra (Bruker MultiRam) were measured to investigate the variation of chemical bonds before and after persodiation. The chemical compositions of samples were determined by ICP-OES (Agilent 730) and EDS (X-Max 50). FIB was used to observe the cross section of active material particles on Tescan SOLARIS equipment. The ssNMR spectra were recorded with a Bruker AVANCE NEO 400 MHz NMR spectrometer.

### Electrochemical measurements

The  $\text{Na}_3\text{VP}$  cathode sheet was fabricated by mixing  $\text{Na}_3\text{VP}$ , Super P and polyvinylidene fluoride at a mass ratio of 80 : 10 : 10 in NMP and further spreading the mixture on the aluminum foil with a doctor blade. After vacuum drying, the electrode was cut into discs with a diameter of 12 mm for use. For half cells, CR-2032-type coin cells were assembled by using pieces of Na foil as the counter and reference electrodes,  $\text{Na}_3\text{VP}$  or  $\text{Na}_4\text{VP}$  as the working electrode, and glass fiber as a separator in an argon-filled glove box with  $\text{H}_2\text{O}$  and  $\text{O}_2$  contents less than 0.1 ppm. The electrolyte was 1 M  $\text{NaClO}_4$  dissolved in ethylene carbonate/diethyl carbonate (1 : 1 v/v) solution with a 5% fluoroethylene carbonate (FEC) additive. Galvanostatic charge/discharge tests were conducted between 2.0 and 4.0 V vs.  $\text{Na}^+/\text{Na}$  on a NEWARE CT4008 cycler battery cycler at room temperature. In particular, the nominal capacity of 1C is  $117.6 \text{ mA g}^{-1}$ . For full cells, all procedures were identical to those for half-cell assembly with the exception of using a hard carbon electrode as the anode. The cathode/anode capacity ratio was set as 1 : 1 and the voltage range was set as 1.5–4.0 V vs.  $\text{Na}^+/\text{Na}$ . The CV measurement was executed on an Admiral electrochemical workstation at a scan rate of  $0.1 \text{ mV s}^{-1}$ . The energy density ( $E$ ) of the full cell was calculated using the following formula:

$$E = Q \times V / (m_{\text{cathode}} + m_{\text{anode}}) \quad (6)$$

where  $Q$ ,  $V$ ,  $m_{\text{cathode}}$ , and  $m_{\text{anode}}$  indicate the discharge capacity and average discharge voltage and the mass of the cathode and anode, respectively.

### Data availability

All the data supporting this study are included in the manuscript and the ESI.<sup>†</sup> Example data sets are available on request.



## Author contributions

J. Q. and M. X. conceived the idea of the study. M. X. contributed to the design of the research and the experimental data analysis. F. Z. and Y. Z. conducted the XRD experiments. C. W. conducted the SEM experiments and related data analysis. X. Z. conducted the ssNMR experiments and the analysis of ssNMR results. X. A. and J. Q. supervised the work. The manuscript was written by M. X. and all authors participated in reviewing the manuscript.

## Conflicts of interest

The authors declare no conflicts of interest.

## Acknowledgements

This work was financially supported by the National Natural Science Foundation of China (Grant no. 22279093, and 22075216), the Natural Science Foundation of Hubei Province, China (Grant no. 2022CFB096) and the Fundamental Research Funds for Central University (Grant no. 2042022gf0005 and 2042021kf0194). We would like to thank the Core Research Facility of CCMS (WHU) and Shiyang Laboratory for access to analytical equipment. We thank Xiaobin Zhou from Shiyangia Lab ([www.shiyangia.com](http://www.shiyangia.com)) for his support on XPS analysis.

## References

- 1 F. Wu, J. Maier and Y. Yu, *Chem. Soc. Rev.*, 2020, **49**, 1569–1614.
- 2 J. Deng, W.-B. Luo, S.-L. Chou, H.-K. Liu and S.-X. Dou, *Adv. Energy Mater.*, 2018, **8**, 1701428.
- 3 Y. Tian, G. Zeng, A. Rutt, T. Shi, H. Kim, J. Wang, J. Koettgen, Y. Sun, B. Ouyang, T. Chen, Z. Lun, Z. Rong, K. Persson and G. Ceder, *Chem. Rev.*, 2021, **121**, 1623–1669.
- 4 N. Yabuuchi, K. Kubota, M. Dahbi and S. Komaba, *Chem. Rev.*, 2014, **114**, 11636–11682.
- 5 C. Zhao, Q. Wang, Z. Yao, J. Wang, B. Sanchez-Lengeling, F. Ding, X. Qi, Y. Lu, X. Bai, B. Li, H. Li, A. Aspuru-Guzik, X. Huang, C. Delmas, M. Wagemaker, L. Chen and Y. S. Hu, *Science*, 2020, **370**, 708–711.
- 6 P. Hu, T. Zhu, C. Cai, X. Wang, L. Zhang, L. Mai and L. Zhou, *Angew. Chem., Int. Ed.*, 2023, **62**, e202219304.
- 7 C. Liu, Z.-X. Zhang, R. Tan, J.-W. Deng, Q.-H. Li and X.-C. Duan, *Rare Met.*, 2021, **41**, 806–813.
- 8 J. Qian, M. Zhou, Y. Cao, X. Ai and H. Yang, *Adv. Energy Mater.*, 2012, **2**, 410–414.
- 9 L. F. Zhao, Z. Hu, W. H. Lai, Y. Tao, J. Peng, Z. C. Miao, Y. X. Wang, S. L. Chou, H. K. Liu and S. X. Dou, *Adv. Energy Mater.*, 2020, **11**, 2002704.
- 10 H. He, Q. Gan, H. Wang, G.-L. Xu, X. Zhang, D. Huang, F. Fu, Y. Tang, K. Amine and M. Shao, *Nano Energy*, 2018, **44**, 217–227.
- 11 J. Qian, X. Wu, Y. Cao, X. Ai and H. Yang, *Angew. Chem., Int. Ed.*, 2013, **52**, 4633–4636.
- 12 Y. Li, X. Lai, J. Qu, Q. Lai and T. Yi, *Acta Phys. – Chim. Sin.*, 2022, **38**, 2204049.
- 13 E. Goikolea, V. Palomares, S. Wang, I. R. Larramendi, X. Guo, G. Wang and T. Rojo, *Adv. Energy Mater.*, 2020, **10**, 2002055.
- 14 C.-X. Yu, Y. Li, Z.-H. Wang, X.-R. Wang, Y. Bai and C. Wu, *Rare Met.*, 2022, **41**, 1616–1625.
- 15 H. He, D. Sun, Y. Tang, H. Wang and M. Shao, *Energy Storage Mater.*, 2019, **23**, 233–251.
- 16 Y. R. Yang, C. Wu, X. X. He, J. H. Zhao, Z. Yang, L. Li, X. Q. Wu, L. Li and S. L. Chou, *Adv. Funct. Mater.*, 2023, 2302277.
- 17 D. Dewar and A. M. Glushenkov, *Energy Environ. Sci.*, 2021, **14**, 1380–1401.
- 18 K. Zou, W. Deng, P. Cai, X. Deng, B. Wang, C. Liu, J. Li, H. Hou, G. Zou and X. Ji, *Adv. Funct. Mater.*, 2020, **31**, 2005581.
- 19 I. Moezz, H. G. Jung, H. D. Lim and K. Y. Chung, *ACS Appl. Mater. Interfaces*, 2019, **11**, 41394–41401.
- 20 H. Wang, Y. Xiao, C. Sun, C. Lai and X. Ai, *RSC Adv.*, 2015, **5**, 106519–106522.
- 21 J. Martinez De Ilarduya, L. Otaegui, J. M. López del Amo, M. Armand and G. Singh, *J. Power Sources*, 2017, **337**, 197–203.
- 22 Y. B. Niu, Y. J. Guo, Y. X. Yin, S. Y. Zhang, T. Wang, P. Wang, S. Xin and Y. G. Guo, *Adv. Mater.*, 2020, **32**, e2001419.
- 23 J. Martínez De Ilarduya, L. Otaegui, M. Galcerán, L. Acebo, D. Shanmukaraj, T. Rojo and M. Armand, *Electrochim. Acta*, 2019, 321.
- 24 R. Zhang, Z. Tang, D. Sun, R. Li, W. Yang, S. Zhou, Z. Xie, Y. Tang and H. Wang, *Chem. Commun.*, 2021, **57**, 4243–4246.
- 25 Z. Jian, Y. Sun and X. Ji, *Chem. Commun.*, 2015, **51**, 6381–6383.
- 26 Y. Liu, X. Wu, A. Moezz, Z. Peng, Y. Xia, D. Zhao, J. Liu and W. Li, *Adv. Energy Mater.*, 2022, **13**, 2203283.
- 27 S. Mirza, Z. Song, H. Zhang, A. Hussain, H. Zhang and X. Li, *J. Mater. Chem. A*, 2020, **8**, 23368–23375.
- 28 J. X. Wu, C. Lin, Q. H. Liang, G. D. Zhou, J. P. Liu, G. M. Liang, M. Wang, B. H. Li, L. Hu, F. Ciucci, Q. Liu, G. H. Chen and X. L. Yu, *Infomat*, 2022, **4**, e12288.
- 29 K. Lin, Q. Liu, Y. Zhou, H. Chen, J. Liu, J.-Z. Zhao and X. Hou, *Chem. Eng. J.*, 2023, **463**, 142464.
- 30 Y.-S. Su and J.-K. Chang, *Batteries*, 2022, **8**, 99.
- 31 M. Xu, M. Liu, Z. Yang, C. Wu and J. Qian, *Acta Phys. – Chim. Sin.*, 2022, **39**, 2210043.
- 32 M. Liu, J. Zhang, S. Guo, B. Wang, Y. Shen, X. Ai, H. Yang and J. Qian, *ACS Appl. Mater. Interfaces*, 2020, **12**, 17620–17627.
- 33 Y. Cao, T. Zhang, X. Zhong, T. Zhai and H. Li, *Chem. Commun.*, 2019, **55**, 14761–14764.
- 34 Y. Shen, J. Qian, H. Yang, F. Zhong and X. Ai, *Small*, 2020, **16**, e1907602.
- 35 M. Liu, Z. Yang, Y. Shen, S. Guo, J. Zhang, X. Ai, H. Yang and J. Qian, *J. Mater. Chem. A*, 2021, **9**, 5639–5647.
- 36 X. Liu, Y. Tan, T. Liu, W. Wang, C. Li, J. Lu and Y. Sun, *Adv. Funct. Mater.*, 2019, **29**, 1903795.
- 37 X. Liu, Y. Tan, W. Wang, C. Li, Z. W. Seh, L. Wang and Y. Sun, *Nano Lett.*, 2020, **20**, 4558–4565.
- 38 C. Wu, J. Hu, H. Chen, C. Zhang, M. Xu, L. Zhuang, X. Ai and J. Qian, *Energy Storage Mater.*, 2023, **60**, 102803.



39 X. Liu, T. Liu, R. Wang, Z. Cai, W. Wang, Y. Yuan, R. Shahbazian-Yassar, X. Li, S. Wang, E. Hu, X.-Q. Yang, Y. Xiao, K. Amine, J. Lu and Y. Sun, *ACS Energy Lett.*, 2020, **6**, 320–328.

40 S. Park, Z. Wang, Z. Deng, I. Moog, P. Canepa, F. Fauth, D. Carlier, L. Crogueennec, C. Masquelier and J.-N. Chotard, *Chem. Mater.*, 2021, **34**, 451–462.

41 R. Thangavel, D. Han, B. Moorthy, B. K. Ganesan, M. Moorthy, Y. Park, K. W. Nam and Y. S. Lee, *Small Methods*, 2022, **6**, e2100888.

42 C. Wei, F. Luo, C. Zhang, H. Gao, J. Niu, W. Ma, Y. Bai and Z. Zhang, *Ionics*, 2019, **26**, 2343–2351.

43 H. Fang, S. Gao, M. Ren, Y. Huang, F. Cheng, J. Chen and F. Li, *Angew. Chem., Int. Ed.*, 2023, **62**, e202214717.

44 J. Jang, I. Kang, J. Choi, H. Jeong, K. W. Yi, J. Hong and M. Lee, *Angew. Chem., Int. Ed.*, 2020, **59**, 14473–14480.

45 G. Wang, B. Huang, D. Liu, D. Zheng, J. Harris, J. Xue and D. Qu, *J. Mater. Chem. A*, 2018, **6**, 13286–13293.

46 B. Paduszek and M. K. Kalinowski, *Electrochim. Acta*, 1983, **28**, 639–642.

47 M. Fujita, A. Ishida, T. Majima and S. Takamuku, *J. Phys. Chem.*, 1996, **100**, 5382–5387.

48 Z. Y. Gu, J. Z. Guo, Z. H. Sun, X. X. Zhao, W. H. Li, X. Yang, H. J. Liang, C. D. Zhao and X. L. Wu, *Sci. Bull.*, 2020, **65**, 702–710.

49 C. Xu, J. Zhao, Y. A. Wang, W. Hua, Q. fu, X. Liang, X. Rong, Q. Zhang, X. Guo, C. Yang, H. Liu, B. Zhong and Y. S. Hu, *Adv. Energy Mater.*, 2022, **12**, 2200966.

50 T. Broux, T. Bamine, F. Fauth, L. Simonelli, W. Olszewski, C. Marini, M. Ménétrier, D. Carlier, C. Masquelier and L. Crogueennec, *Chem. Mater.*, 2016, **28**, 7683–7692.

51 G. Yan, S. Mariyappan, G. Rousse, Q. Jacquet, M. Deschamps, R. David, B. Mirvaux, J. W. Freeland and J. M. Tarascon, *Nat. Commun.*, 2019, **10**, 585.

52 Z. Jian, C. Yuan, W. Han, X. Lu, L. Gu, X. Xi, Y.-S. Hu, H. Li, W. Chen, D. Chen, Y. Ikuhara and L. Chen, *Adv. Funct. Mater.*, 2014, **24**, 4265–4272.

53 S. C. Yin, H. Grondy, P. Strobel, H. Huang and L. F. Nazar, *J. Am. Chem. Soc.*, 2003, **125**, 326–327.

